Supporting Information for
Deformation evolves from shear to extensile in rocks due to energy optimization

Text S1.

To quantify the accelerating dominance of the extensile fractures, we compare the proportion of differential stress, σ_D, steps in which there is a greater volume of extensile fractures than shear fractures throughout the full experiments, i.e., $r > 1$, and within the final 90% to 95% of the σ_D / σ_D^F. This proportion for the full experiment ranges from 0.04 (WG18_14) to 0.95 (WG10) (**Figure** S5), with a mean and standard deviation of 0.29 and 0.35, respectively. The experiment with the lowest applied confining stress (σ_2=5 MPa, WG10) experiences a higher proportion of σ_D with $r > 1$ than the experiments with higher applied confining stress, even for the experiments with the same effective stress. Consequently, the confining stress appears to be the primary control on the type of deformation, rather than the effective stress.

Except for the experiment with σ_2=5 MPa (WG10), all of the experiments host an increase in the proportion of extensile fractures from the final 90% to 95% of the normalized σ_D (**Figure** S5). In these experiments, the mean ± one standard deviation of the proportion of σ_D increases from 0.26 ± 0.15 to 0.42 ± 0.11 in the final 90% to 95% of the normalized σ_D.

The damaged rocks experience larger changes in the proportion of σ_D with $r > 1$ preceding failure than the intact rocks. The damaged rocks increase the proportion of σ_D by 0.14-0.40, while the intact rocks increase the proportion of σ_D by 0.07-0.10 (**Figure** S5). This result occurs in part because the damaged rock WG18_14 produces a larger volume of fractures than the intact rock deformed at the same effective stress (**Figure** S6). However, the volumes of fractures that develop at the end of experiments WG19_18 and WG06_02 are similar to each other (**Figure** S6), and yet the damaged rock WG06_02 hosts a larger proportion of σ_D with $r > 1$ when the normalized σ_D is > 95% than the intact rock WG19_18. These experiments have about the same proportion of σ_D when σ_D > 90% of the normalized σ_D, and so the damaged rock hosts a faster increase in the proportion of σ_D than the intact rock. Consequently, all but one of the experiments experience an increasing proportion of σ_D in which they host a greater volume of extensile fractures than shear fractures, and the damaged rocks experience larger changes in this proportion from the final 90% to 95% of the σ_D at macroscopic failure.

Experiment name	Confining stress (MPa)	Fluid pressure (MPa)	Effective stress (MPa)	Intact or damaged (heat-treated)
WG10	5	0	5	Intact
WG19_18	10	5	5	Intact
WG06_02	10	5	5	Damaged
WG20_19	15	10	5	Intact
WG18_14	15	10	5	Damaged
WG14	20	10	10	Intact

Table S1. Confining stress, fluid pressure, effective stress, and amount of preexisting damage in each experiment. The damaged Westerly granite samples were heated in an oven in order to produce preexisting fractures. We heated them first with a heating rate of 4°C/minute from room temperature to 650°C, and then them for five hours at 650°C, and then cooled them with a cooling rate of 4°C/minute to room temperature. All deformation experiments were performed at ambient room temperature in the range 22-24°C.

Poisson’s ratio		0.2
Young’s modulus		70 GPa
Sliding and static friction of faults		0.65
Properties of intact rock elements that propagate from fractures		
	Sliding friction	0.65
	Slip weakening distance	0.01 mm

Table S2. Mechanical and frictional properties of the intact rock and fractures in the numerical models. The mechanical properties of the intact rock, the Young’s modulus and Poisson’s ratio, are values typical for intact granite (e.g., Haimson & Chang, 2000). The sliding and static coefficient of friction of fractures are representative of faults within granite (e.g., Savage et al., 1996). We vary the shear and tensile strengths, and internal friction coefficient of the intact rock elements (**Table** S3).

	Shear strength (MPa)	Tensile strength (MPa)	Internal friction coefficient
Parameter set #1	10	2	0.65
Parameter set #2	10	2	0.85
Parameter set #3	10	2	1.00
Parameter set #4	25	5	1.00

Table S3. Combinations of tensile strength, shear strength and internal friction coefficient of the intact rock at the edges of fractures tested here. The properties of the intact rock elements represent the nominally intact, but heavily damaged, rock at the tips of preexisting fractures. The tested internal friction coefficients are within the range measured for nominally intact granite (Scholz, 2019). The minimum tested internal friction coefficient is the static and sliding friction coefficient of the preexisting fractures in the models (0.65) because rocks do not have an internal friction coefficient that is lower than the sliding or static friction coefficient. The ratio of the tensile and shear strength for low porosity, crystalline rocks is generally 1:5 (Paterson & Wong, 2005). For low porosity, nominally intact, crystalline rocks such as granite, the inherent shear strength ranges from 50-100 MPa, and the tensile strength ranges from about 5-20 MPa (Zhang, 2022; Paterson & Wong, 2005; Liu et al., 2021). Following the approach of Fattaruso et al. (2022), we selected the values of 2 MPa and 10 MPa, and 5 MPa and 25 MPa for the tensile and shear strengths because the rock near the tips of growing fractures is heavily damaged, and thus the strength of this rock is much lower than the bulk tensile and shear strength measured for intact granite samples. These values determine whether a newly added element will fail at a given level of differential stress, and thus may influence the direction of growth from a propagating fracture tip.

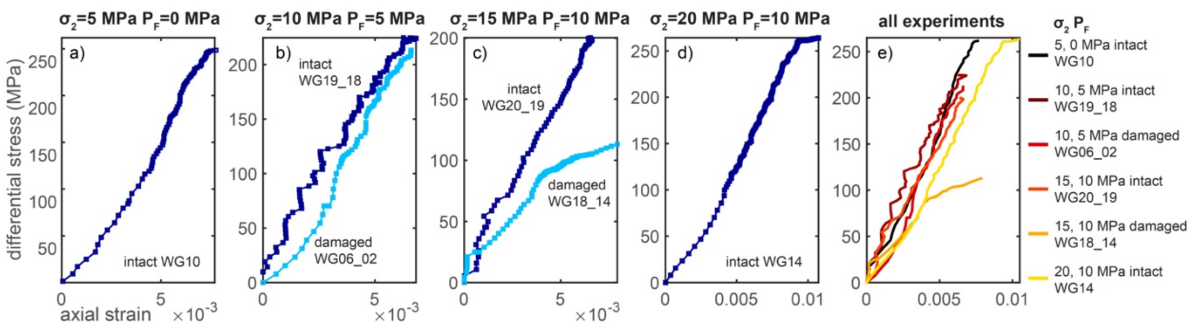

Figure S1. Differential stress and axial strain conditions when each X-ray tomogram was acquired in each experiment for a given set of loading and fluid conditions (a-d), and all of the experiments (e). The conditions of each experiment are listed at the top of the plots in (a-d). The dark blue and light blue curves indicate experiments performed on intact (non-heat-treated) and damaged (heat-treated) rocks, respectively.

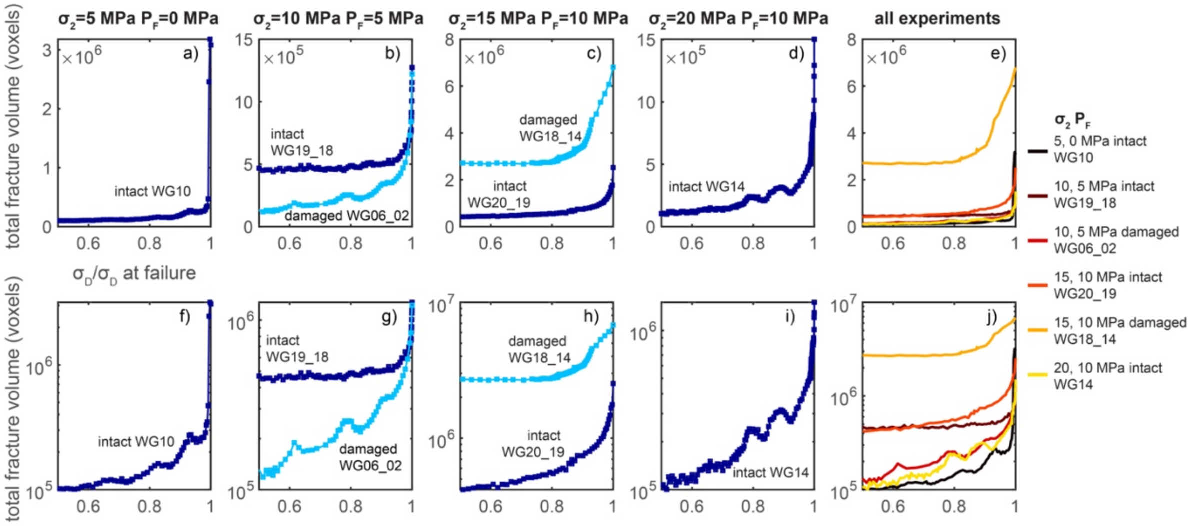

Figure S2. Evolution of the total fracture volume (number of voxels) in each experiment in linear plots (a-e) and log-linear plots (f-j) in terms of the differential stress, σ_D, normalized to σ_D at macroscopic failure. All of the experiments show sharp increases in the total volume of fractures after about 90% of the σ_D at failure. The fracture volume consistently increases in some experiments (WG19_18, WG18_14, WG20_19). In contrast, the other experiments show temporary episodes in which the total fracture volume decreases (WG10, WG06_02, WG14). These decreases occur because increasing differential stress can close fractures. For the experiments with σ_2=10 MPa and P_F=5 MPa (b, g), the damaged rock has less total fracture volume than the intact rock from the onset of loading until >98% of the σ_D at failure. Then, immediately preceding macroscopic failure, the damage rock develops about the same fracture volume as the intact rock. In contrast, for the pair of experiments with σ_2=15 MPa and P_F=10 MPa (c, h), the damaged rock hosts a larger volume of fractures throughout the experiment than the intact rock.

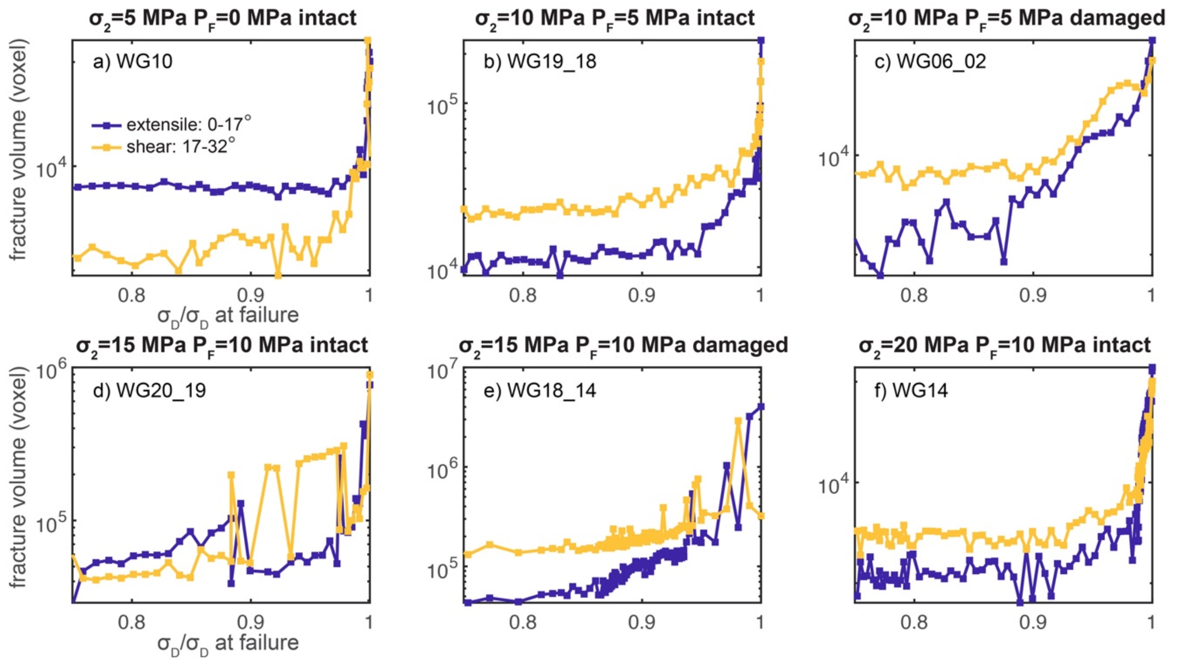

Figure S3. Evolution of the total fracture volume within the ranges of extensile-dominated (θ=0-17°) and shear-dominated (θ=17-32°), v_θ, as a function of the σ_D normalized to the σ_D at macroscopic failure for each experiment. The evolutions of v_θ show similar trends to the total fracture volume (Figure S2): relatively constant values until an acceleration after about 90% of the σ_D at macroscopic failure. For some portions of each experiment, the volume of extensile fractures is larger than the volume of the shear fractures, i.e., the blue curve is above the yellow curve. To compare the volume of each class of fractures more precisely, we track the ratio of the volume of the extensile fractures to the volume of the shear fractures (**Figure** 3).

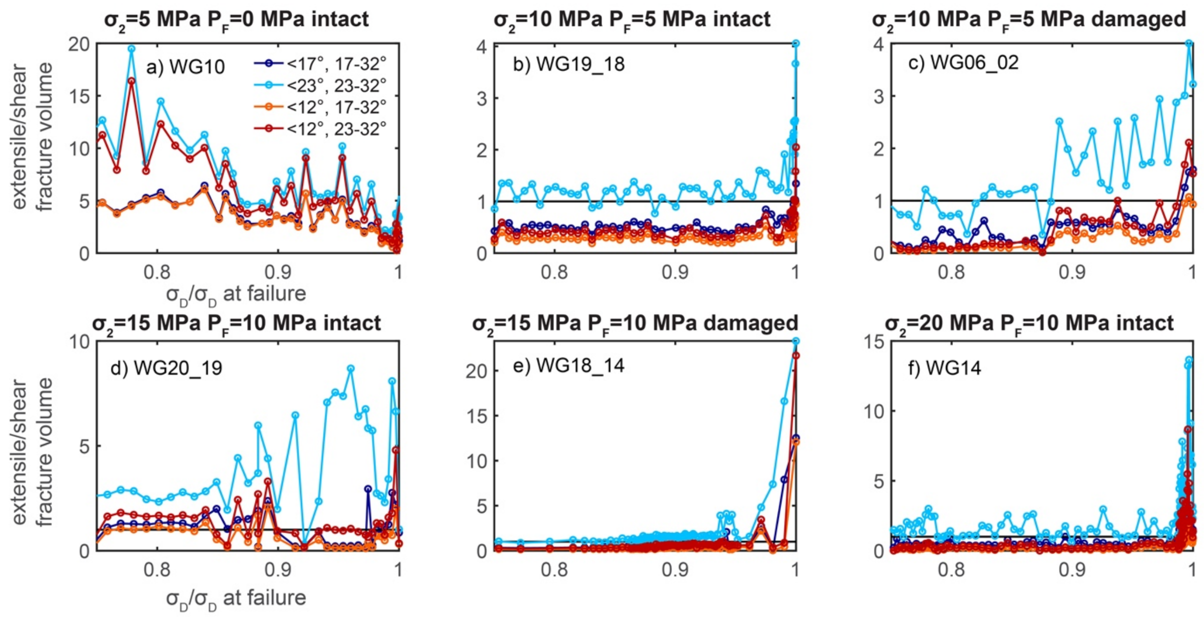

Figure S4. Evolution of the proportion of the volume of the extensile and shear fractures, v_θ, as a function of the σ_D normalized to the σ_D at macroscopic failure for each experiment using different ranges of the extensile and shear fractures. When the ratio of the v_θ for the extensile fractures to the shear fractures, r, is greater than one, then the rock hosts a larger volume of extensile fractures than shear fractures. The colors of the curves indicate the combination of extensile and shear orientations used to calculate the ratio: 1) extensile-dominated fractures are θ_e=0-17° and shear-dominated fractures are θ_s=17-32° (dark blue), 2) θ_e=0-23° and θ_s=23-32° (light blue), 3) θ_e=0-12° and θ_s=17-32° (orange), and 4) θ_e=0-12° and θ_s=23-32° (dark red). Using different combinations of orientation ranges does not change the general trend of the curves for each experiment, except for the experiment WG20_19 and the angle ranges of #2. In the other experiments, all of the combinations produce a similar trend with an increasing volume of extensile fractures toward failure (WG19_18, WG06_02, WG18_14, WG14), or extensile-dominated deformation throughout loading (WG10). For the remaining experiment (WG20_19), using the orientation ranges of θ_e=0-23° and θ_s=23-32° produce a higher volume of extensile fractures than shear fractures throughout loading than the other orientation ranges. However, for all of the combinations, the volume of extensile fractures increases toward failure after about 97% of the σ_D at macroscopic failure. The consistent trends of r with increasing σ_D for the four different combinations lend confidence to the results described in the main manuscript using θ_e=0-17° and θ_s=17-32°.

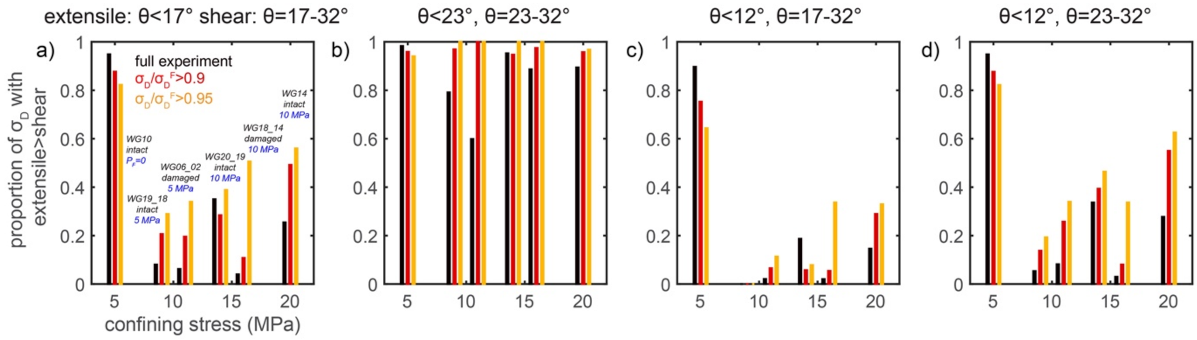

Figure S5. Proportion of the differential stress, σ_D, in which the volume of extensile fractures is larger than the volume of shear fractures: when r is greater than one for each experiment throughout loading (black bars), within the final 90% (red bars) and 95% (orange bars) of the σ_D at macroscopic failure using different ranges of angles for the extensile and shear fractures: a) θ_e=0-17° and θ_s=17-32°, b) θ_e=0-23° and θ_s=23-32°, c) θ_e=0-12° and θ_s=17-32°, and d) θ_e=0-12° and θ_s=23-32°. Each group of bars represents one experiment. The horizontal axis lists the applied confining stress. The general trends described in the main manuscript with the angle ranges of θ_e=0-17° and θ_s=17-32° (a), are similar to the trends observed for the other angle ranges (b-d) except for the ranges of #2 (b). Using a larger range of orientations considered to be extensile fractures leads to higher proportions of σ_D in which the volume of extensile fractures is larger than the volume of shear fractures. This trend is expected. The general trend of an increasing volume of extensile fractures relative to shear fractures with increasing differential stress is similar regardless of the angle ranges used. The exception to this trend is the experiment with the lowest confining stress, consistent with the results shown in the main manuscript.

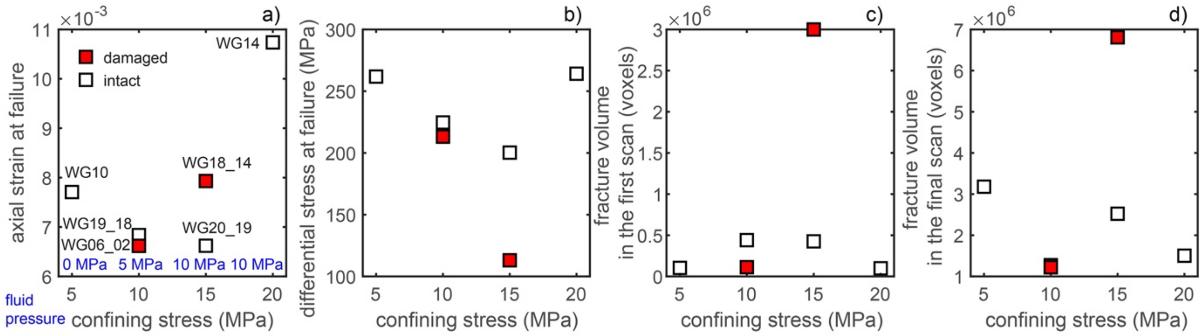

Figure S6. The axial strain (a), differential stress (b) and total fracture volume (d) in the scan acquired immediately preceding macroscopic failure, and the total fracture volume (c) in the first scan acquired, at the onset of the differential stress loading for the six experiments. The horizontal axis indicates σ_2, and the blue text in (a) indicates the P_F. The experiment names are listed in (a) near the corresponding symbol. The red and white squares indicate the experiments performed on damaged and intact rock, respectively. The fracture volume is reported in terms of the number of voxels. The intact rocks fail at larger differential stresses than the damaged rocks when σ_2=10 MPa and 15 MPa (b). When σ_2=10 MPa and P_F=5 MPa, the intact and damaged rocks accumulate similar amounts of axial strain and differential stress preceding macroscopic failure (a-b). These experiments also host a similar volume of fractures in the final scan acquired immediately preceding macroscopic failure (d). In contrast, for the pair of experiments with σ_2=15 MPa and P_F=10 MPa, the damaged rock fails at a lower differential stress (b) and accumulates more axial strain (a) than the intact rock. The damaged rock (WG18_14) also hosts a larger volume of fractures at the beginning (c) and end of the experiment (d) than the intact rock (WG20_19). Similarly, the intact rocks deformed at σ_2=5 MPa, P_F=0 MPa (WG10), and σ_2=20 MPa, P_F=10 MPa (WG14) fail at larger differential stresses and accumulate less total fracture volume than the damaged experiment WG18_14. In summary, the fracture volume that the rock accumulates preceding macroscopic failure positively correlates with the axial strain and differential stress that the rock can host preceding macroscopic failure: higher fracture volume produces higher accumulated axial strain and lower differential stress at failure.

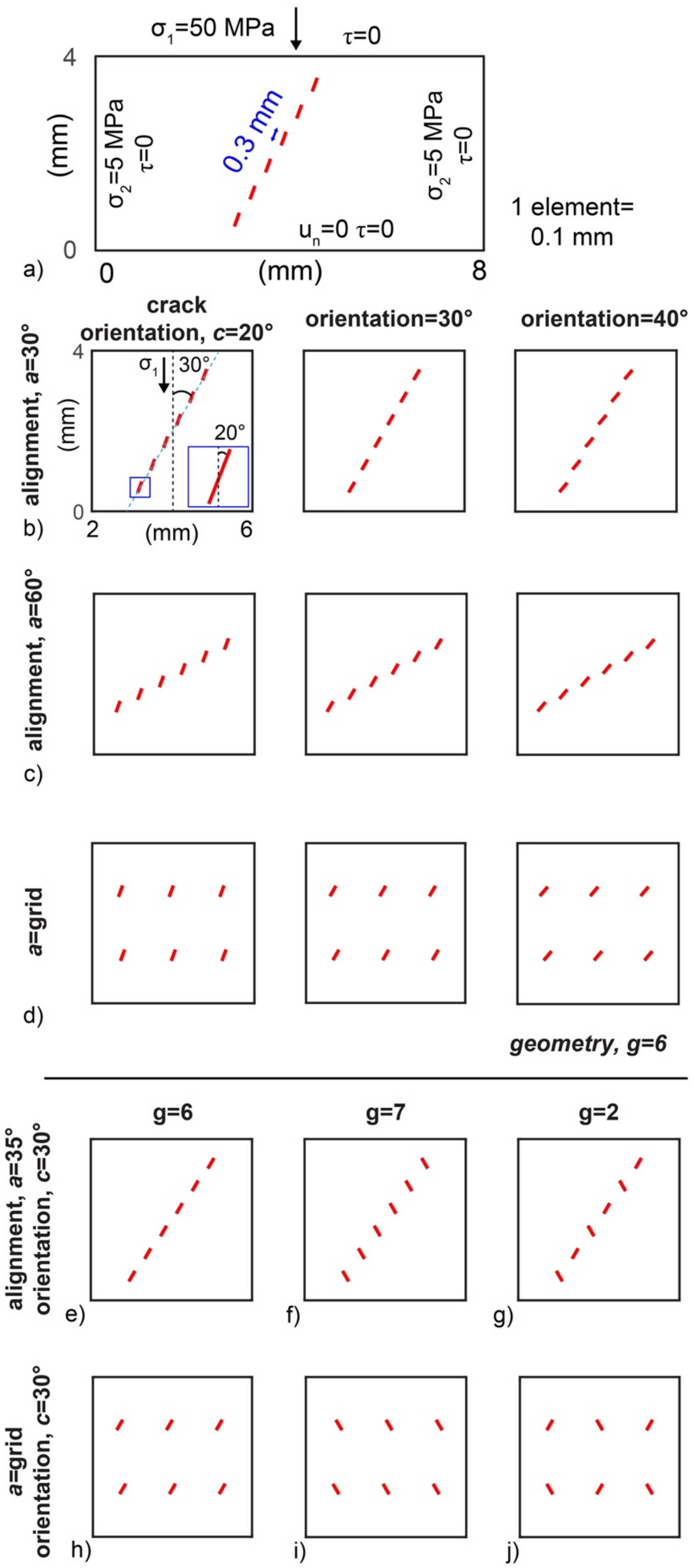

Figure S7. Model set-up (a) and example fracture geometries tested in the first stage of fracture growth (b-j). We apply the σ_2 of the majority of the experiments, and we apply the lowest σ_1 that allows the fractures to slip, or 50 MPa in the first stage of fracture growth. The shear stresses, τ, are zero on all the sides of the model. The normal displacement, u_n, is zero on the bottom side of the model so that the model does not move in space. We select the length of the fractures using the ratio of the length of the longest six fractures in the experiments at σ_1 = 50-60 MPa, and the rock cylinder height, such that the ratio in both systems is near 0.1. The crack orientation, *c*, is the orientation of the individual fractures relative to the σ_1 direction (b). The alignment, *a*, is the orientation of the array of the six fractures relative to the σ_1 direction (b). We vary the alignment from 10 to 90°, and also include a grid pattern of the fractures, in which they are equally distributed through the central portion of the model domain, from 2-6 mm from the left size (d). The geometry, *g*, indicates the combination of the sign of the dips of the fractures. For example, when *g*=6, the signs of all the fractures are positive, and they all dip to the right (e). When *g*=2, the signs of the dip alternate from positive to negative (g).

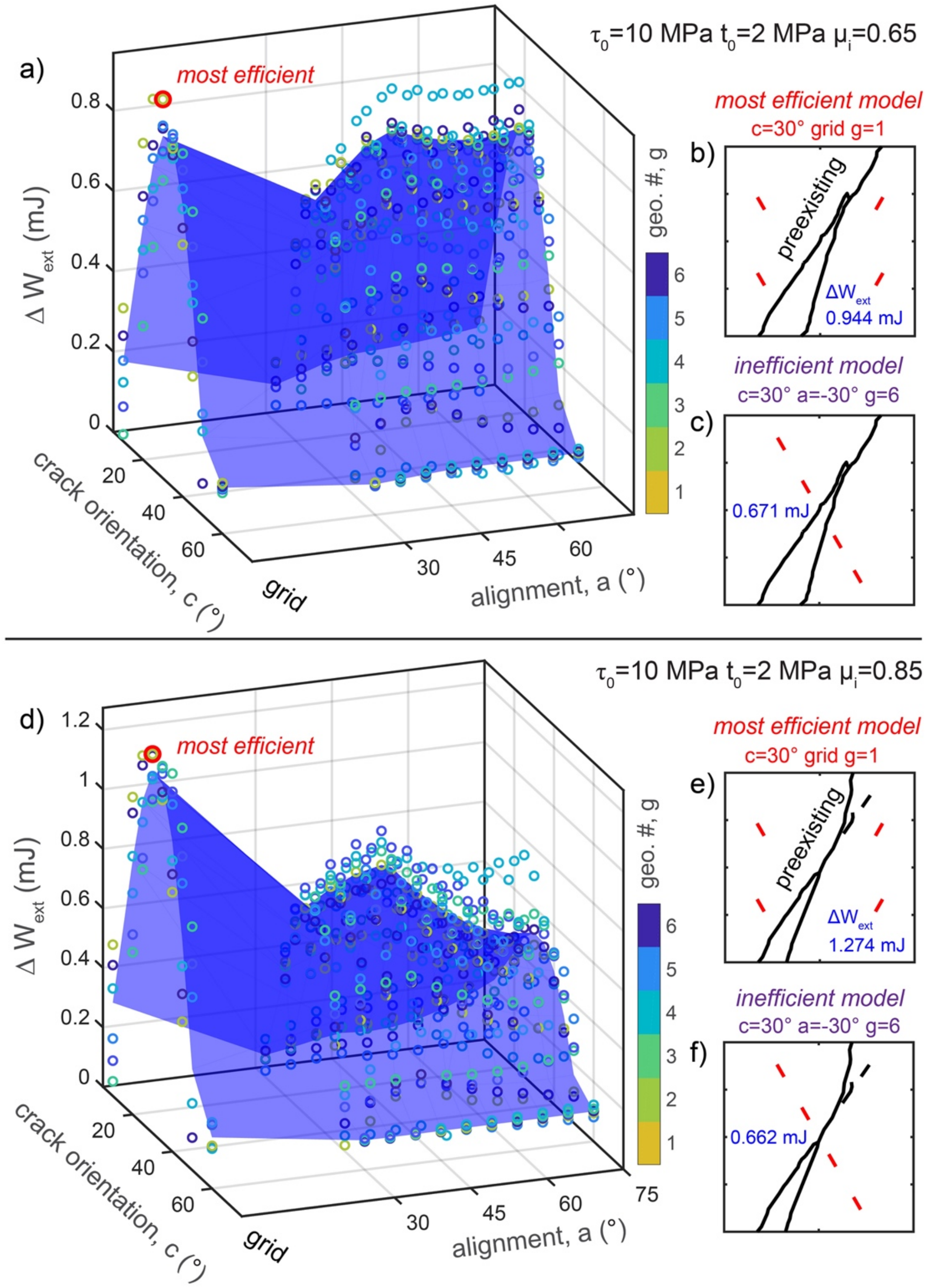

Figure S8. Constraints from linear elastic numerical models on the geometry of the fracture network in rocks under triaxial compression following the coalescence of an array of fractures using a shear strength, τ_0=10 MPa, tensile strength, t_0=2 MPa, and internal friction coefficient, μ_i=0.65 for the intact rock near the edges of fracture tips (a-c), and with the same strength parameters and μ_i=0.85 (d-f). a, d) Three-dimensional plot shows the ΔW_{ext} produced by models with selected crack orientations, c, macroscopic alignments, a, and geometries, g, the combination of the varying sign of the dip of the fractures. The models that produce the largest ΔW_{ext} are the most mechanically efficient, and thus most likely to form. The colors of the symbols indicate the g. The most efficient geometry is highlighted with red circle in the three-dimensional plot, and shown in (b) and (e). (c) and (f) show examples of inefficient geometries. Blue text shows the ΔW_{ext} for the geometry. The most efficient model includes fractures arranged in a grid pattern (b, e), rather than an aligned array of fractures (c, f).

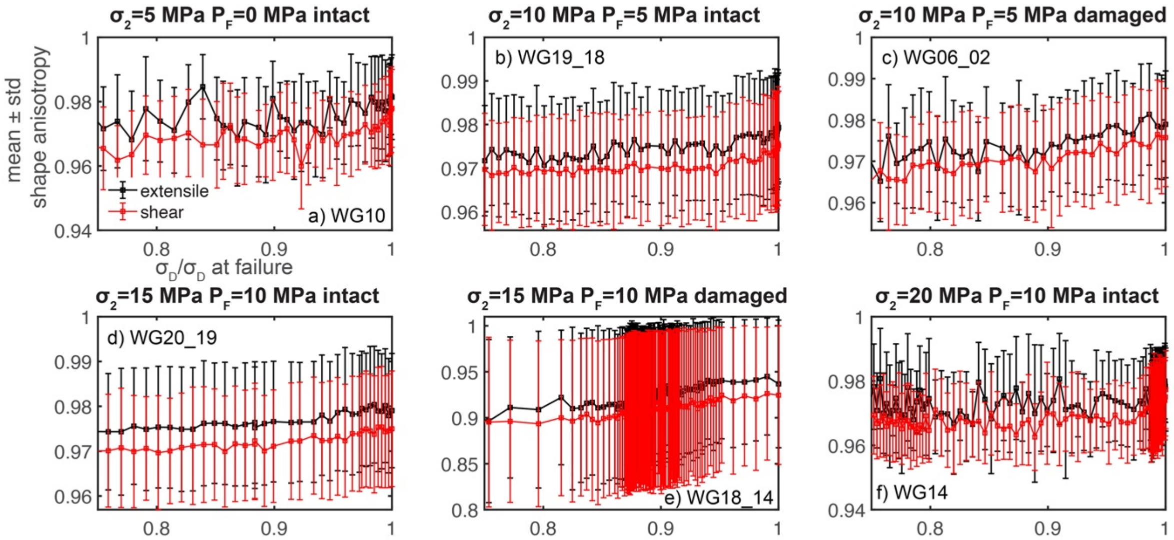

Figure S9. Comparing the shape anisotropy of the extensile (θ=0-17°) and shear (θ=17-32°) fractures. The shape anisotropy is one minus the shortest/longest eigenvalues of fractures, and thus thinner fractures have anisotropies closer to one. A potential observational bias may exist that favors the detection of extensile fractures rather than shear fractures. If such a bias exists, then the anisotropy of shear fractures would be higher than the anisotropy of extensile fractures. However, the data reveal the opposite trend: the anisotropy of the extensile fractures are similar or slightly larger than shear fractures. This result indicates that an observational bias does not favor the detection of the extensile fractures in the X-ray tomography data. The similarity of the shape of the extensile and shear fractures also suggests that the volume of the fractures is the most appropriate proxy for the influence of each mode of deformation on the system.

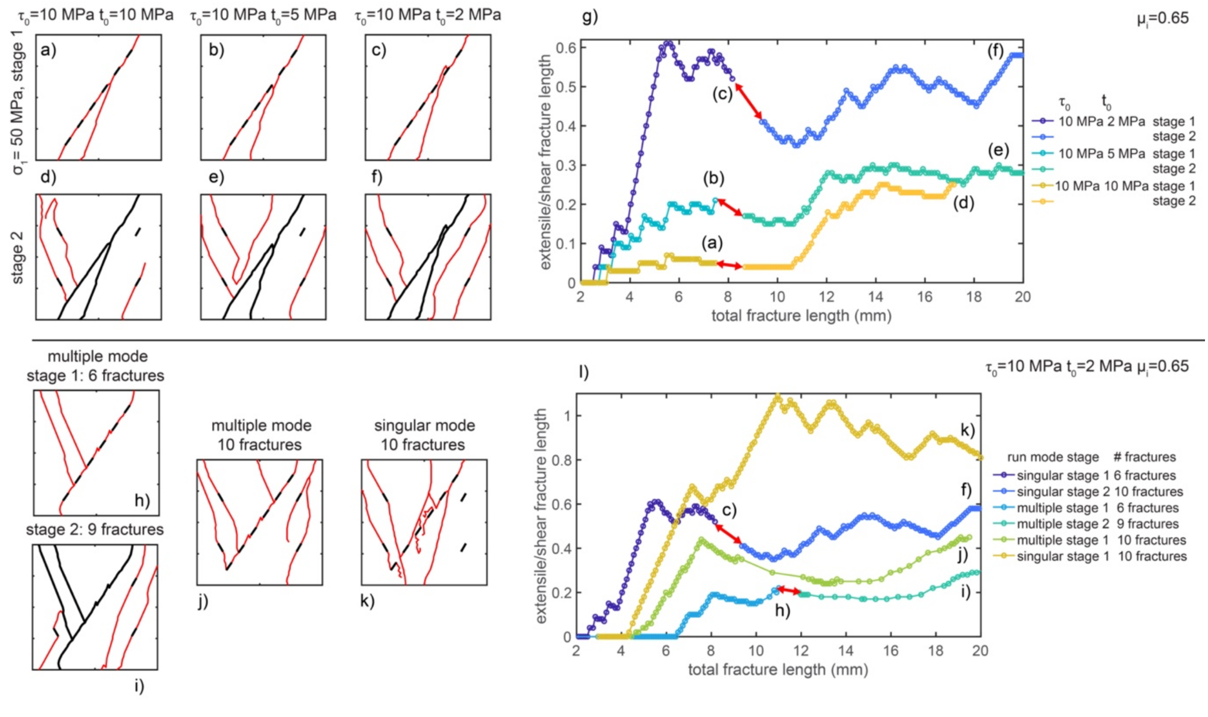

Figure S10. Testing the influence of the shear strength, τ_0, and tensile strength, t_0 (a-g), the run mode of GROW, and the inclusion of all ten fractures at the beginning of the simulations (h-l) on the evolution of the proportion of extensile to shear fractures. All of the models have an internal friction coefficient of μ_i=0.65. The τ_0 of all the models is 10 MPa, and the t_0 decreases from 10 MPa (a, d), 5 MPa (b, e), to 2 MPa (c, f). The value of t_0=2 MPa is the most realistic value, based on experimental measurements of the tensile and shear strength, and the main manuscript focuses on these results accordingly. Increasing t_0 decreases the maximum extensile/shear fracture length that the models achieve by the end of the simulation. However, even when t_0 equals τ_0, the amount of extensile deformation increases with fracture growth (g), consistent with the experiments. Varying the run mode of GROW from the singular version, in which only the fracture with the highest combination of mode I and mode II stress intensity factor grows at each time step, to the multiple run mode version, in which several fracture tips may grow in one time step, produces changes in the fracture geometry propagated by GROW (h-k), but does not change the overall evolution of the proportion of extensile/shear fracture length (l). Regardless of the run mode, or if the models include six or ten fractures at the beginning of the simulation, the amount of extensile deformation increases with fracture growth (l). The complex geometry of the fractures shown in (k) develops because the fractures continue to propagate in locally isotropic stress fields after the through-going fractures develop.

References

Fattaruso, L., Cooke, M., & McBeck, J. (2022). The Influence of Fracture Growth and Coalescence on the Energy Budget Leading to Failure. Frontiers in Earth Science, 589.

Haimson, B., & Chang, C. (2000). A new true triaxial cell for testing mechanical properties of rock, and its use to determine rock strength and deformability of Westerly granite. International Journal of Rock Mechanics and Mining Sciences, 37(1-2), 285-296.

Liu, Y., Huang, D., Cen, D., Zhong, Z., Gong, F., Wu, Z., & Yang, Y. (2021). Tensile strength and fracture surface morphology of granite under confined direct tension test. Rock Mechanics and Rock Engineering, 54(9), 4755-4769.

Savage, J. C., Byerlee, J. D., & Lockner, D. A. (1996). Is internal friction friction? Geophysical research letters, 23(5), 487-490.

Scholz, C. H. (2019). The mechanics of earthquakes and faulting. Cambridge University Press.

Zhang, Z. X. (2002). An empirical relation between mode I fracture toughness and the tensile strength of rock. International journal of rock mechanics and mining sciences, 39(3), 401-406.